Performance and Calibration of the Nadir Suomi-NPP Ozone Mapping Profiler Suite from Early-Orbit Images

*C. Pan[1], M. Kowalewski[2], R. Buss[3], L. Flynn[4], X. Wu[4], M. Haken[5] and M. Caponi[6]

* 1 ESSIC, University of Maryland, College Park, MD 20740; 2 USRA, Columbia, MD; 3 Raytheon, Riverdale, MD 20737; 4 NOAA STAR, College Park, MD 20740; 5 SSAI, Lanham, MD 20706; 6 Aerospace Corporation, El Segundo, CA 90245

ABSTRACT

The Ozone Mapping Profiler Suite (OMPS) was launched aboard the Suomi National Polar-orbiting Partnership (S-NPP) spacecraft on October 28, 2011. A successful thorough Early Orbit Checkout (EOC) enabled the current Intensive Calibration and Validation (ICV) stage. We present our analyses and results of OMPS Nadir early-orbit sensor performance and calibration. We collected and analyzed data from both nominal and diagnostic activities via orbital measurements of detector dark current, sensor linearity, and solar irradiance. Our results demonstrate that the OMPS Nadir sensor smoothly transitioned from ground to orbit by meeting or exceeding sensor level requirements. The orbital measurements agree with the predicted values determined during the prelaunch calibration and characterization of OMPS. Our results also suggest that the influence of "hot" overactive pixels and other effects of charge couple device (CCD) lattice damage due to energetic particle hits onto the CCD must be accounted for in the dark current calibration.

Index Terms— OMPS, CCD, calibration

1. INTRODUCTION

OMPS is one in a series of ozone monitoring sensors flown by NOAA and NASA [1]. It continues more than 30 years of global ozone monitoring by providing data products of ozone in the Earth's atmosphere. The OMPS sensor suite comprises three instruments [2]: a Nadir Mapper (NM), a Nadir Profiler (NP) and a Limb Profiler (LP). The Nadir system, which is the topic of this paper, has a common telescope with two grating spectrometers that provide a spectral sampling of 0.4 nm and 1 nm full-width half-maximum (FWHM) spectral resolution. The NP covers the wavelength range from 250 to 310 nm using 146 spectral channels and the NM covers 300 nm to 380 nm using 196 spectral channels. In Earth observation mode, the OMPS cross-track NP and the NM fields of views (FOVs) are co-bore sighted to 0.1 degrees (3-sigma level), where the NP has a 16.7° cross-track FOV providing ozone profiles in a single ground swath of 250x250 km at nadir, while the NM has a 110° cross-track FOV, providing ozone total column measurements in 36 ground cells across a 2800 km Earth view swath with a spatial resolution of 50 x 50 km at nadir. An algorithm for binning CCD pixels separately in each sensor provides flexibility of variable numbers of spatial cells in the FOVs that allows the sensors to achieve and provide higher resolution products. Table 1 summarizes OMPS Nadir system nominal properties and specifications.

Table 1: OMPS Nadir System Properties and Specifications

Nadir System	Two separate grating CCD spectrometers (Nadir Mapper and Nadir Profiler)
Swath Width	Mapper: 2800 km
	Profiler: 250 km
Field of View (FOV)	Mapper: 110 x 0.27 deg
	Profiler: 16.7 x 0.25 deg
Spectral Range	Mapper: 300 to 380 nm
	Profiler: 250 to 310 nm
Spectral Sampling Interval	Mapper: 2.4 pixels per FWHM
	Profiler: 2.4 pixels per FWHM
Spectral Resolution	Mapper: 1.0 nm
	Profiler: 1.0 nm
CCD Focal Plane Array (FPA) Cooling	Thermo-Electric Coolers (TECs)
	Mapper operational set point: -30.0 C
	Profiler operational set point: -45.0 C
Calibration	LEDs for linearity and gain correction. Dual solar reflective diffusers maintain calibration stability. Data binning algorithm attains flexibility in the spatial IFOV.

The OMPS focal plane arrays (FPAs) consist of dual two-dimensional CCD optical detectors that are used for each spectrometer to provide a response to photons within the spectral range. A CCD row of pixels runs vertically, and a column runs horizontally.
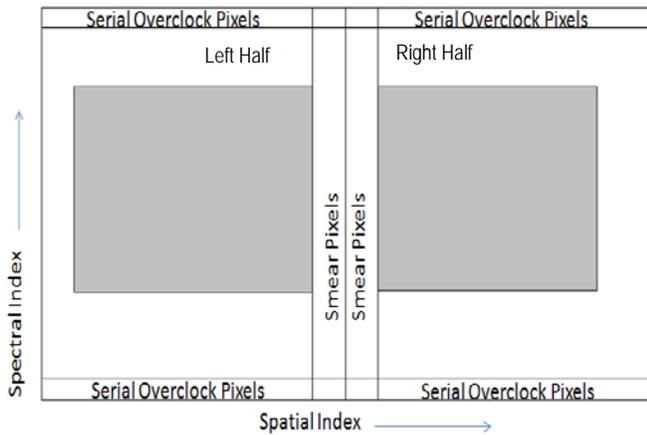
Fig. 1: Schematic diagram of OMPS NM dual CCD readout full frame image format. The gray area is the CCD photoactive region cast by the OMPS optics and pixel sampling.

Fig. 1 is a diagram of the NM full frame CCD readout consisting of 340 spectral columns by 740 (2 x 370) spatial rows for the NM cross-track, plus 2 x 12 serial over-clock pixels at each edge in the vertical and 2 x 20 parallel over-clock smear pixels in the horizontal direction in the middle of Fig. 1. The OMPS NM potential total readout size is thus 780 rows x 364 columns, which is used often for calibrations such as the dark current and LED Lamp linearity measurements. With flexible sampling and binning of pixels by summation, actual images can be smaller, as often is used for Earth data. Nominally for the NM, the spectral range spans sampled pixels from 101 to 296 as counted from the bottom, for a total of 196 contiguous pixels.

The NP functionally uses only one of the CCDs, the left one, to record its smaller FOV. Thus, the NP CCD has 340 pixel spectral columns and each horizontal column consists of 370 spatial pixels on a CCD. Calibrations are usually full-frame, but the sampled spectral range for Earth measurements uses just 147 contiguous pixels starting at spectral pixel 119.

For collecting CCD image data, the pixels collect signal during commanded integration times. These pixels are transferred within a short transfer time period to CCD storage regions (not shown in Fig. 1) on each side of the photoactive regions, and then processed horizontally, line by line, through CCD read-out amplifiers. The read-out register extends beyond the CCD edges by 12 serial over-clock pixels in the spectral direction on the top (trailing) and 12 on the bottom (leading) of the CCD, as well as 20 smear pixels in the spatial direction for one CCD. These over-clocked pixels are used to estimate electronic offsets and define the dark current and image smear during the CCD read-out and transfer time periods. The over-clock pseudo pixels are read together with every CCD column and then combined with the CCD image to form the larger data readout image depicted in Fig. 1.

Each CCD has its own amplifiers and set of primary and secondary electronics for converting the CCD electrons analog signal to digital photon counts. For launch, engineers configured the sensors to use primary electronics, whose bias is captured by the top serial over-clock pixels. The sensor's logic processor numerically collects one or more images of the same type, co-adds the images, samples the readout array, discarding non-active pixels outside the sampled photoactive region, and then sums the specified pixel counts into spatial bins that are each called a macropixel or spatial cell. In contrast, the sensors never bin the spectral pixels, which are always at full spectral resolution and practically the same for the NP and the NM.

To conserve the telemetry data rate during normal operations with Earth integration times of 7.48 sec., and to provide a 3.15 degree Nadir Mapper instantaneous field of view (IFOV) at nadir during Earth observations, pixels in each NM column are spatially binned into 38 macropixels, including 36 cross-track spatial cells, and two binned smear macropixels each consisting of the central 16 of the possible 20 pseudo pixels. A NM Earth macropixel typically consists of 20 individual pixels but the first and last edge macropixels have 22 and 26 pixels, respectively. The central two Earth macropixels are 12 and 8 pixels each, which are combined later in the ground processing into a single macropixel.

For the NP sensor nominal observing the Earth, all of the active 94 spatial pixels are binned into one macropixel to match the NP cross-track IFOV to the central five NM macropixels. The nominal NP Earth integration of 37.4 sec. coincides with 5 successive NM swaths along track. Both NP and NM Earth data are normally acquired simultaneously through the same aperture, overlap in space, and coincide in time. In contrast, though OMPS NP solar data is taken simultaneously with some NM solar data, in general, the NP and NM calibrations can be performed separately. In any case, it is important to note the calibrations normally and habitually are at a higher pixel sampling than the nominal Earth data in order to provide reliable and accurate calibrations. Pre-launch laboratory sensor characterizations by the Ball Aerospace fabricator provided us with original wavelength, radiance, and irradiance calibrations for converting counts to physical units for both pixel and macropixels.

After being built by Ball Aerospace Technology Corporations and launched by NASA on Oct 28, 2011, OMPS was successfully activated and passed functional tests designed by the builder. After those tests, in which the CCD FPAs reached thermal stability (Table), the OMPS on-orbit calibration and validation proceeds through the EOC and ICV phases. Currently, OMPS is in the ICV stage, an extension of the sensor checkout period. There is no clear

delineation between the EOC and ICV because some of the measurements require repeating so that some analyses may not be complete at the end of a phase. During each phase, OMPS activities are primarily catalogued into routine calibration, special calibration, diagnostic, and performance, some of which could be done internally with the aperture closed. OMPS opened its aperture door on January 26, 2012, beginning its Earth observing mission. During the EOC and ICV, we performed internal consistency checks of sensor parameters and instrument behavior to identify sensor anomalies. We collected and analyzed data from all types of activities to extract sensor level trends and features about the in-flight detector performance.

Through analyses of the early data, we determined the initial settings for the onboard sensor parameters, sensor calibration tables, and ground processing tables. Consequently, we have established the orbital OMPS calibration in accordance with the actual sensor behavior. For evaluating the sensor performance in its transition from ground to orbit, we compared the in-flight OMPS dark, electronic bias, linearity and solar irradiance with the prelaunch predicted values. Our results show that orbital OMPS performance is as stable as expected and that the orbital established calibration sequences are well suited to determine sensor characteristics. We derive dark current, electronic bias, system linearity, and verify that the solar irradiance falls within the sensor dynamic range. Finally, the current OMPS ICV period will end when its products are validated and then OMPS calibration activities will change to routine monitoring.

2. OVERVIEW OF ON-ORBIT CALIBRATION

The orbital OMPS calibration is performed through measurements of dark current, linearity, solar irradiances, and earth radiances [3]. The Nadir OMPS sensor suite has four onboard calibrators: two Light-Emitting Diodes (LEDs), one each in the NM and NP, as well as two common Solar Reflective Diffusers (working and reference) deployed at different positions. The LEDs are used to provide the linearity calibration, and the diffusers are used to maintain wavelength and radiometric calibration trending by periodically observing the Sun. The diffusers act as a door to the aperture: closed for LED and dark measurements; opening for a view of the Earth. The OMPS Earth-view radiances are normalized by the observed solar irradiances at the same wavelengths to an accuracy of greater than or equal to 2% at all wavelengths from 250-380 nm [4]. For nominal earth observation, science data is collected during the portion of the S-NPP polar orbit on the sunlight side from solar zenith angle -88 degrees to +80 degrees (solar zenith angle is defined zero at the Earth equator at noon time, positive when the satellite is in the North, and negative in the Southern hemisphere) and solar calibration data is collected over the North Pole from solar zenith angle +80 deg. to +100 deg., then followed by

collection of linearity and dark current images on the dark side of the Earth with the Nadir diffuser in the closed position.

2.1 Dark Currents and Electronic Biases

Each CCD effectively has its own calibrations: two for the NM and one for the NP. The cooling of the focal planes (Table 1) ensures relatively stable dark currents isolated from orbital thermal fluctuations in the sensors. Our OMPS dark calibration defines the average dark current for each CCD pixel in both the image and storage regions of a CCD FPA. Particularly, the calibration estimates the dark current during the readout time period, and when used as subtraction, removes CCD electronic bias and bad pixels from image data. The electronic bias of a CCD is the count level read by the readout amplifier in the CCD signal chain when no signal is applied. The bias level depends on amplifier gain, and it is added to the measured signals by the OMPS Main Electronics Box (MEB) to prevent negative voltages at the analog-digital convertor input. The calibrated dark current and bias are two of the key sensor parameters applied by the operational data processing code on sensor data to correct the sensor raw counts prior to applying radiometric calibration coefficients. To obtain the true counts from the radiance, C_{Jk} corrections to observed macropixel counts O_{Jk} at Earth integration time t_E are performed by subtracting CCD raw dark current D_{jk} for pixel j, k, (rows binned N_D through N_J) at a potentially different dark integration time t_D, electronics offset B and raw smear S_k of column k (rows 1 through N_S),

$$C_{Jk} = O_{Jk} - \sum_{j=N_D}^{N_J} \frac{t_E}{t_D}(D_{jk} - B) - [S_k - \sum_{j-1}^{N_S} \frac{t_E}{t_D}(D_{jk} - B)] \quad (1)$$

where a JK denotes a macropixel from pixel N_D through N_J and a jk denotes a single pixel.

Orbital OMPS dark current measurements are normally made on the eclipse side of the orbit with the entrance aperture of the sensor blocked. The original lab and initial orbital dark measurements consisted of a consecutive series of 100 individual dark 1.2471 sec. frames collected and co-added by the sensor into a single image of 124.71 seconds total integration. However, the orbital OMPS dark current that we present in this paper was significantly impacted by transient detector events, mostly due to cosmic particle hits in a high radiation region. (A detailed description is provided in Section 3.1.) Thus, for future corrections to dark current, we have devised a new standard dark calibration process with better temporal resolution to detect and isolate transients. By manually assembling separate 1.2471 sec. single-frame measurements into one time-averaged image, we discard those frames contaminated by transients to obtain an image whose effective integration time is 72 sec. instead of 124.71 sec.

2.2 System Linearity

The OMPS electronic system exhibits nonlinearity, which is a result of a chain of amplifiers, including the on-chip CCD amplifier, the pre-amp board amplifiers, and the amplifiers in the MEB. For calibrating the linearity that are associated with each CCD readout, an LED lamp in each sensor is used to illuminate the entire FPA, for example both CCDs for the NM. The absolute intensity of an LED is relatively unimportant, only that the LED be stable while illuminating the CCDs. Moreover, the system nonlinearity of the stable electronics is not expected to change much while OMPS is orbiting, but correction of the nonlinearity is required via sensor specifications that dictate 1) the nonlinearity of Nadir sensor shall be no more than 2% of full well; 2) the total LED output drift shall be less than 1% per minute after a 5 minute LED lamp warm-up period; and 3) the high-frequency LED current variability shall be less than 0.1% RMS. The system nonlinearity η is defined by,

$$\eta = \frac{(Q_m - Q_i)}{Q_{max}} \quad , \quad (2)$$

where Q_m is the measured response to a LED measurement input, Q_i is the ideal response to the Q_m, and Q_{max} is the full well response.

The non-linearity does not depend on wavelength, only on the count levels as distributed over the sampled pixels, denoted by the index i over a total of n to pixels. The residual uncertainty in the nonlinear response curve is defined by the standard deviation expressed as a percentage,

$$\sigma = \left[\frac{1}{n-2} \sum_{i=1}^{n} \left(\frac{Rad_i^{meas} - Rad_i^{fit}}{Rad_i^{meas}} \right)^2 \right]^{1/2} * 100\%. \quad (3)$$

The variable Rad_i^{meas} is the measured source radiance in pixel i. Rad_i^{fit} is a linear fit derived from the bias-corrected counts multiplied by radiance coefficients at pixel i.

The planned orbital OMPS linearity calibration is performed once per week, and the resulting linearity correction is made during Earth observations when the OMPS flight hardware corrects signals in each pixel for non-linearity prior to coadding the CCD readouts and binning into macropixels. Using the measured count level in a pixel, and the linearity calibration table, the sensor linearly interpolates between the calibrated ideal counts to obtain the corrected linear counts in a pixel. In contrast, linearity corrections to the dark measurements and solar measurements are applied by the ground system data processing only after the data are telemetered down. For these data, however, the ground processing system uses the same linearity calibration table and interpolation correction as for the Earth observation.
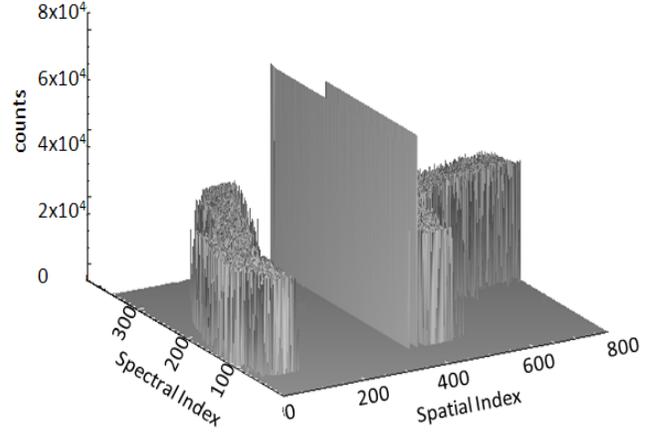
Fig. 2: One of the orbital NM LED images used in the linearity calibration. The pixels, including smear over-clock ones, were collected with the prelaunch defined LED sample table specific to the NM. The integration time of this image this 0.48 sec.

The on-orbit linear measurements are currently conducted once a month due the sensor has extremely stabled linearity. Following the same method to determine linearity in the lab, allowing the LED lamp to warm for five minutes, we monitor and correct an orbital OMPS linearity response through an analysis of LED lamp signals measured in a series of stepped integration times. The NM and NP measurements are the si except for the sample tables and LEDs. A linearity calibration measurement sequence collects 41 ramp images (ex. Fig. 2) with the integration time stepped from 0 to 2.4 sec. in 60 ms increments to obtain different output signal levels that span the dynamic range of a CCD. However, 42 reference measurement full-frame images (similar to Fig. 3) with 0.5 sec. fixed integration time are interleaved in observation sequence with the pixel-sampled ramp images (Fig. 2) in order to compensate for any drifts in the LED intensity.

Fig. 2 shows one of the 83 images collected at 0.48 sec. integration time with a sensor builder predefined LED sample table, as well as the higher smear regions dividing the two CCDs. The sample table is determined such that it excludes the bright and bad pixels and includes a sufficient sampling of spectral columns (101 to 296) with differing full well depths to sample the linear portion of the illumination pattern in the spectral dimension.

One complicating factor in the linearity calibration is the illumination uniformity of the LED lamp, which is located directly in front of the CCD FPA to provide a relative stable internal illumination with highly linear pixel quantum efficiencies. Fig. 3 is a representative all-pixel LED image collected from the orbiting OMPS NM 0.5 sec. reference measurement. The image at the small-scale exhibits slight variations, which we tentatively attribute to inhomogeneities in the LED lamp itself. At the large-scale, the LED illumination varies from the lower right to the left.
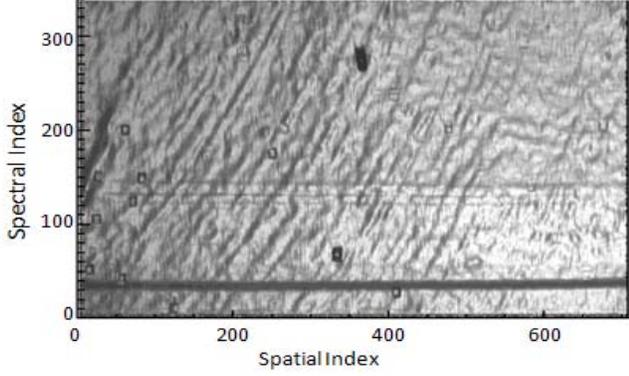
Fig. 3: A representative NM CCD all-pixel frame LED image showing the orbital lamp illumination fine-scale and large-scale features. To depict the actual CCD pixels, bias and smear over-clock pseudo-pixels have been omitted.

We minimize both of these types of non-uniformities by adopting an appropriate LED sample table that excludes most of the inhomogeneous pixels but which includes those pixels with similar illuminations. Outside of the effective view region, there is a horizontal dark stripe at the lower part of the image on spectral column number 3-4, which is an image of an optic filter edge projected onto the CCD detector surface, and has no influence on the calibration due to the adopted pixel sampling.

2.3 Solar Observation

The orbital OMPS solar calibration observations are made via a reflective working diffuser for short-term monitoring and via a reflective reference diffuser at the telescope entrance aperture for long term monitoring of sensor stability. The working diffuser is deployed once every week to provide observed solar irradiances, as well as to monitor changes in sensor spectral wavelengths, spectral band-passes, and radiometric sensitivities. The reference diffuser is nominally deployed every six months to monitor the stability of the working diffuser. During a measurement, the diffuser moves through seven different positions to cover the entire NM sensor FOV of 110 degrees. Fig. 4 shows a diagram of seven solar diffuser positions. Position 4 illuminates the entire NP FOV of 16.7 degrees.

The measured orbital solar irradiance, F^m_{jk} can be written as,

$$F^m_{jk}(t) = \frac{C^i_{jk} k^i_{jk}}{g \, \rho(t) \tau_{jk}(t)} \qquad (4)$$

The measured $C^i_{jk}(t)$ refers to the solar irradiance i counts of pixel jk that have been corrected for the nonlinearity, dark, electronic bias, and image transfer smear; k^i_{jk} is the irradiance i calibration constant derived from prelaunch calibration at pixel j,k; $\tau_{jk}(t)$ stands for sensor throughput changes (τ ($t=0$) = 1); $\rho(t)$ is the solar diffuser plate reflectivity (ρ ($t=0$) = 1); and g is the sensor relative angular irradiance response (goniometry), which varies spatially and
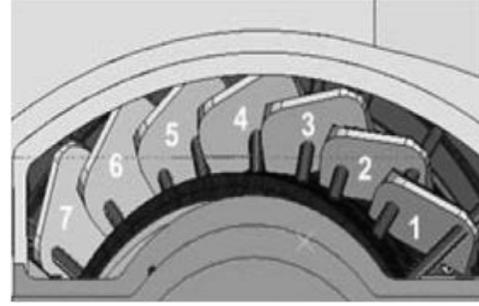
Fig. 4: Diagram of seven solar diffuser positions in OMPS Nadir solar measurement (courtesy of Ball Aerospace Technology Corporations).

spectrally from pixel to pixel with a value of 1 at the angle at which radiometric calibrations were performed prior to launch.

The goniometry calibration coefficients are a set of 40 x 40 grids at varying azimuth and elevation angles for each diffuser position and diffuser type, and the grids were established during sensor prelaunch calibration and characterizations. Because the angles at which the orbital solar irradiances strike and reflect off the diffusers vary from measurement to measurement, linearly interpolated values from the grids are applied to solar images to account for variations in irradiance sensitivity. Interpolation of a grid, when compared to a Lorentzian functional fit, indicates that a goniometric correction may have errors that we estimate to be up to 1% for individual pixels.

As measured in the laboratory, Fig. 5 shows the NM nadir view goniometry distribution for wavelength channel 310 nm at diffuser position 5. The azimuth angle ranges from $12.3^{\circ} \sim 31.8^{\circ}$ degrees and the elevation ranges from $1.39^{\circ} \sim 7.41^{\circ}$ degrees in sensor goniometry coordinates.
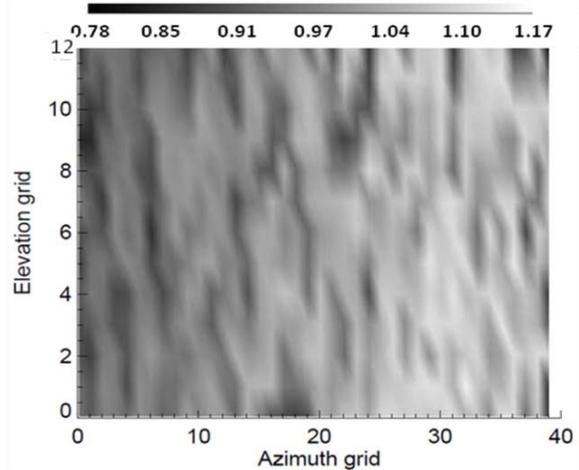
Fig. 5: OMPS NM goniometry distributions at the working diffuser position 5 for wavelength 310 nm. Other wavelengths have different patterns of distribution as a function of sensor yaw and pitch angles described as azimuth and elevation, respectively, in goniometeric coordinates.

The angular distribution response in Fig. 5 exhibits undesirable small-scale irregularities from a diffuser that should have only uniform large-scale features that capture the overall angular dependence. The irregularities likely stem from the surface roughness of the aluminum surface so that the incident light is not uniformly diffused after reflection. Thus, the larger the span of angles covered by an observation, the more uniform the illumination.

The solar calibration is challenging because the set of measurements is so time consuming that all of the initial nominal measurements were made within a single orbit, resulting in a limited angular coverage by a diffuser over all seven positions. The solar data collected for each diffuser position have a rolling decrease in intensity at either end of the spatial direction, which we wished to mitigate.

To improve the declining signal features, we established a new set of solar measurements that changes the sequence of the initial calibration measurements by extending the measurement angles. The new measurement set is acquired over three consecutive orbits so that the range of measured angles is within the range used to determine the goniometry in the prelaunch calibration performed by the sensor vendor. As a result, the solar irradiance accuracy improved by ~ 0.2% on average compared to the originally measurement sequences.

2.4 Wavelength Shifts

The orbital OMPS spectral registration includes a correction for Doppler shifts caused by OMPS satellite motion toward the Sun during solar measurements, and a calibration that detects any instrument-induced spectral shifts in the solar measurements. During operational processing of the raw solar data, the Doppler shifts are computed from the geolocation and known orbital parameters. The OMPS solar wavelength calibration determines spectral shifts of the band center wavelengths and monitors Full width at half maximum (FWHM) spectral resolution by periodically comparing the observed solar spectrum with a standard solar spectrum [5].

The pre-launch standard solar spectrum of 0.01 nm resolutions originates from ground [6] and balloon [7] data normalized to absolutely calibrated irradiances from the UARS satellite [8] measured on 15 April 1993. For the OMPS Nadir wavelengths, the standard spectrum, covering wavelengths longer than 249.25 nm, is accurate to 0.002 nm for one standard deviation [9].

The correction for instrumental wavelength shifts in Earth spectra is made by extrapolating in time the band center wavelengths derived from several solar wavelength calibrations just prior to the terrestrial observations. Due to thermal fluctuations in the sensor optical bench, the Earth spectra are subjected to intra-orbital wavelength shifts, but our analysis (section 3.10) indicates these shifts are less in absolute magnitude than 0.013 nm, and less in the standard

deviation over all wavelengths than the pre-launch required 0.01 nm of the spectral registration error allocation.

3. PERFORMANCE AND CALIBRATION RESULTS

3.1. Dark Calibration

Fig. 6 shows spectrally averaged dark current of the NM after smear correction for individual spatial indices of the two NM CCD halves, rows 1 to 370 for one CCD half, and 411 to 780 for the other. The orbital dark images are from measurements made outside of the Southern Atlantic Anomaly (SAA) region, roughly -50 < latitude < 0 and -90 < longitude < 40 of increased radiation due to Earth magnetic field irregularity. Compared with the prelaunch data (dash line), the orbital data (solid line) show a similar trend along the spatial direction but with relatively larger magnitudes in signals and variations. An offset in the middle of the data results from potentially different dark currents in the two CCDs, but in practice, tiny errors in subtracting the different electronic biases of about 741 and 779 counts (per readout of each 1.247 sec. image) in the two CCD halves could also cause the discontinuity.
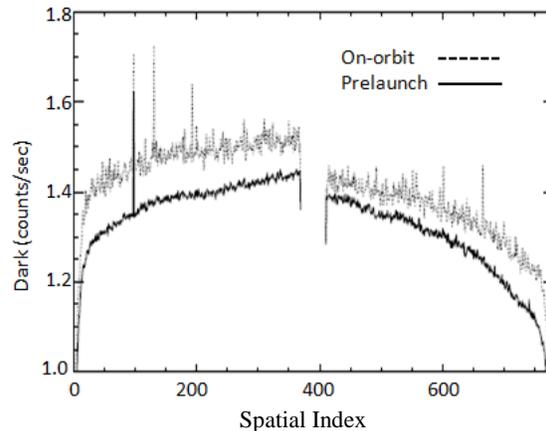
Fig. 6: Spectrally averaged NM dark current after smear correction for all sampled spatial rows (values of smear rows from row number 371 - 410 are excluded). Data were collected during sensor functional tests from ground on March 23, 2011 and from orbit on Nov. 8, 2011, each with a total integration time of 124.7 sec.

Raw dark current, including smear collected during the image readout, is a function of spatial indices and can be estimated by a linear fit to the column averaged dark current along all spatial indices. Fig. 7 shows the NM spatially averaged dark current, after smear charge and electronic bias correction, versus spectral indices for prelaunch (solid and dot lines) and orbital (dashed and dashed-dot lines) images. The corrected dark signals show a nearly flat trend with wavelength channels, indicating that smear charge during frame shift is effectively removed. In general, OMPS on-orbit dark current measured outside the SAA exhibits higher values than the prelaunch data.
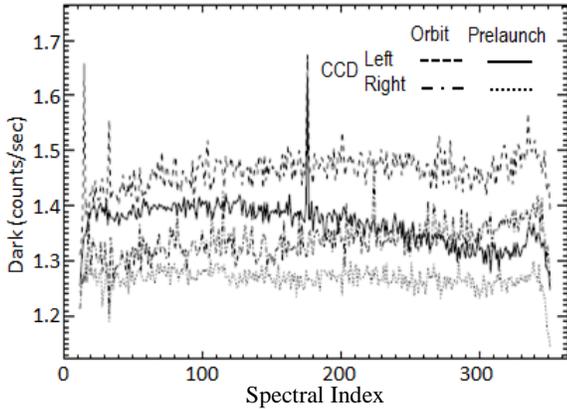
Fig. 7: The NM spatially averaged dark current after smear correction along all spectral indices. Darks are from prelaunch image data (solid and dot lines for the left and right CCDs, respectively) and orbital image data (dashed and dot-dashed lines for the left and right CCD halves, respectively). Data were collected during sensor functional test from ground on March 23, 2011 and from orbit on Nov. 8, 2011 with integration times each of 124.7 seconds and 100 image coadds.

Fig. 8 shows pixel distributions of dark images collected from prelaunch and on-orbit measurements. The on-orbit data distribution has the right tail extended 6.1% higher than the dark mean, indicating a gradually degraded CCD detector performance. To understand interplay between radiation effect and the CCD degradation, we introduce a parameter of "hot pixel" to monitor changes of the radiation-induced dark current in CCDs: a "hot pixel" is any pixel with a statistically significant increase in dark current to the first image after launch, so that the change in the dark current is attributable to the in-flight increase of the number of hot pixels. The level of the change in the dark depicted in Fig. 8, this far in the mission, is within our prediction in section 3.2.

Our interpretation of slightly increasing dark current due to hot pixels is also supported by Fig. 9, where we collect from the two NM CCD detectors those orbital dark diagnostic and dark nominal data having two different integration times of 120 and 72 seconds. The data values from all pixels have been congregated to extract general trends about in-flight evolution of a constant increase in the dark currents. The averaged NM dark signal outside the SAA region increases near linearly by ~ 12% for the first 260 days since launch, suggesting that daily updates of the dark values used for corrections to the Earth and Sun data is desirable in the early orbit stage of the S-NPP mission. The OMPS NP has a similar trend with increases in the mean dark count of about 15% for the first 260 days on-orbit.

Besides the gradual increase in dark counts, the spikes that one observes in Fig. 9 originate from only those dark images measured inside the SAA region, thus reinforcing the evidence that high-energy transient events within the CCD
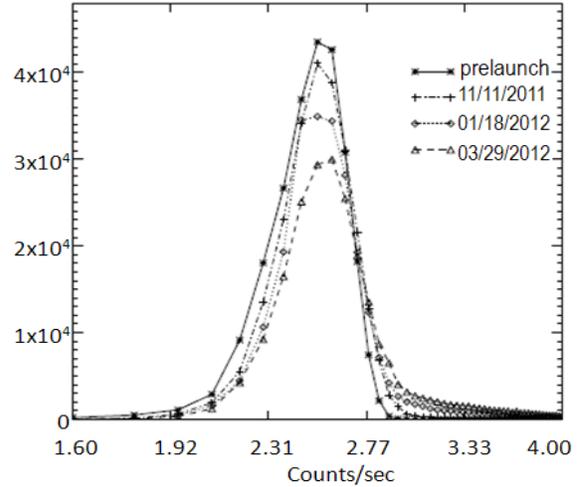
Fig. 8: Histogram of NM dark current shows a distribution of dark signal gradually shifts to a higher mean value with the right tail stretched.
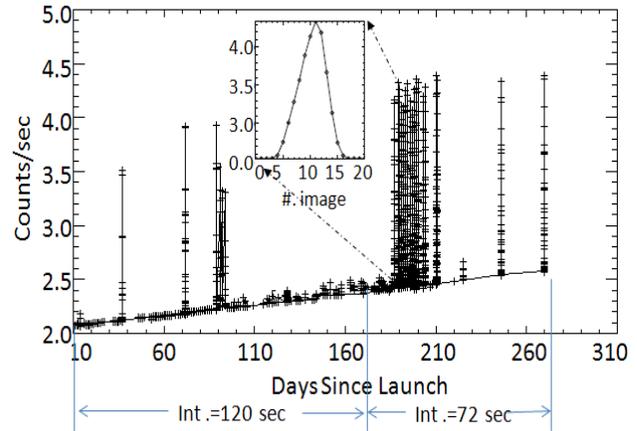
Fig. 9: Pixel-averaged NM dark signals constantly increase about 0.1% daily, indicating a slowly degraded CCD performance mainly caused by hot pixels. The insert shows a typical temporary increase in the dark rate as the sensor transits the SAA.

detectors are causing the increasing normal dark current measured outside the SAA. The impact of the SAA transients on the dark and Earth view radiance is discussed in section 3.3.

The OMPS dark signals also show a strong dependency with the CCD temperature when we deliberately vary the normally stable focal plane temperature of the NM. A 0.01 degree change in the CCD temperature can result in measureable changes in dark signal. However, the few orbital datasets collected early in the mission are not sufficient to be a quantitative measurement of the dark current temperature dependency, but rather they provide an estimate of whether the measured dark current is affected by a 0.02 degree fluctuation in the CCD temperature. In our estimation, when the NM CCD temperature increases from -30.06 to -29.98 degrees, the overall dark current increases about 3%. The bias and linearity are external to a CCD.

The dark current rate was also monitored via diagnostic dark image data that we collected using multiple integration times while the sensors' aperture was closed during the EOC phase. Dark current diagnostic data were taken at nearly all points of the orbit, including day and night sides. We corrected these darks for bias and smear charge and then linearly fit the rates to calculate a slope that represents the dark current generation rate for each half of the CCD focal plane. For the purposes of this analysis, we dropped measurements that were made while the spacecraft was in the SAA region.

Table 2 summarizes the average dark rates from the EOC period and compares them with values from pre-launch tests. Counts are converted to electrons by gain factors (section 3.5). The standard deviation (STD) of the NM EOC dark rate is much larger than NP due to the higher slope in the dark rate trend. The NM dark rate is, and has been historically, higher than NP in large part due to the warmer operating temperature of the focal plane. All instruments show a small linear increase over time in both CCD halves of their respective focal planes. This change, especially in NM, is due to an increasing number of individual pixels becoming "hot" due to radiation damage. Overall, the dark rates are consistent with pre-launch test values and are significantly below the system requirement.

Table 2: NPP OMPS CCD Averaged Dark Rate [e-/sec]

Sensor	CCD	Pre-Launch	On-orbit	
		Mean	Mean	STD
NP	Left	11.3	10.8	1.9
NM	Left	96.2	98.5	13.4
	Right	92.5	97.5	13.2

3.2 Hot Pixels

The performance of CCDs is permanently degraded by total ionizing dose (TID) and displacement damage effects. The TID produces threshold voltage shifts on the CCD gates, and displacement damage reduces the charge transfer efficiency, increases the dark current, and creates random telegraph noise in individual pixels. In addition to these long term effects, cosmic ray and trapped proton transients also interfere with device operation on orbit. In order to have a relevant assessment of in-flight CCD dark degradation, especially concerning the TID and charge transfer efficiency effects, we define a hot pixel that has dark signal above a predetermined threshold even after a detector gain correction. The threshold is set as 8 sigma of the first dark image collected on orbit.

Fig. 10 shows that the number of hot pixels increases constantly with time in orbit. The number of the hot pixels
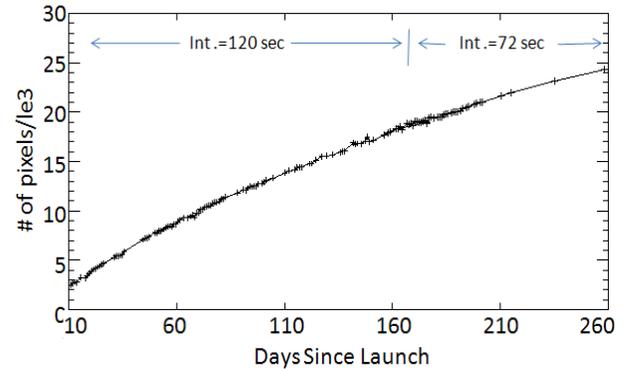
Fig. 10: The number of NM hot pixels increases with time, indicating a gradually degraded CCD detector performance due to radiation effects in orbit.
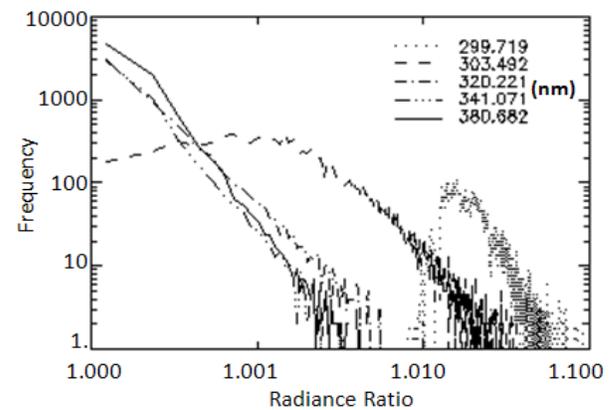
Fig. 11: Histograms of NM Earth radiance ratios for 5 different wavelengths channels. A radiance ratio is derived from corrections using initial dark versus later dark currents to the same Earth image. Changes in the ratio from 1.000 indicate that the changing dark level due to more hot pixels must be monitored with time for properly correcting Earth images.

increases at a rate of ~11 per orbit for the NM and 15 for the NP, indicating a gradually degraded CCD detector performance, causing an average of 11-14% increase in dark signal since launch. The change in the dark due to hot pixels could create up to 10% errors in a calculation of earth view radiances outside of the SAA region, if no correction for changes to the dark is made for the first 150 days on-orbit - when the OMPS team declared the sensor data record product as Beta mature. We expect the number of hot pixels to continue increasing with mission time.

For each representative wavelength, Fig. 11 shows a histogram of the radiance ratio between the day-one dark current corrected radiance to the real-time dark corrected radiance that was retrieved from OMPS NM measurements. The retrieved radiances come from a set of 400 Earth images that we observed on April 06, 2012 covering longitudes from -179.95 to 179.89 degrees and latitudes from -80.52 to 80.4 degrees. The dark data used for the earth view correction is collected on Nov. 11, 2011 and April 06, 2012, respectively. The resulting changes in Fig.

11 of the ratio from unity demonstrate the errors that are produced by using a constant dark current to process the Earth images, which was the case for much of the first year of operationally mass produced Earth radiances. It is noted that due to the NM dichroic filtering contamination, wavelengths below 305 nm are not used in the retrieval algorithms. For now the error are relatively small due to the low dark currents, but for the following years, the dark current will be updated regularly to provide a better correction to the Earth images as the dark currents grow with time.

3.3 SAA Impact

The OMPS CCDs have detected many high-energy transient events associated with solar or cosmic particle impacts. The distribution of these events is a strong function of location, with enhancements in the Polar Regions and particularly in the SAA Region. These events affect single or multiple pixels and result in elevated count levels that raise Earth view macropixel derived radiances higher than the real radiances. For example, Fig. 12 shows a dark image collected during a SAA passage where the average raw dark signal is about 2.5 counts per second, but an individual transient has a spike that reaches 1500 counts/sec.
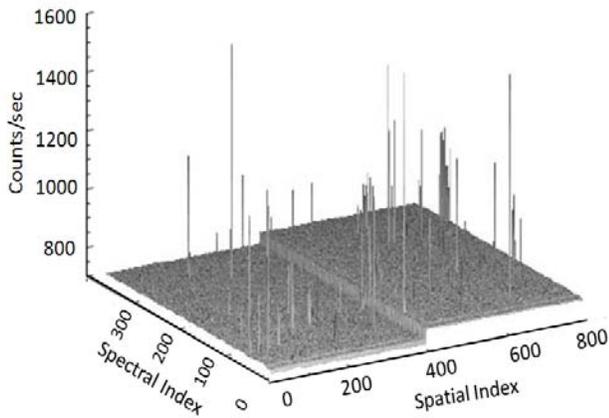
Fig. 12: A typical NM dark image collected when the spacecraft was inside the SAA region. Spikes on the image results from transients caused by energetic particles.

In fact, the SAA region has various levels of trapped protons that produce different transient signal levels, as shown in a subfigure in Fig. 9 where the averaged dark signal gradually increases to nearly 5.0 count/sec and then decreases when the spacecraft is crossing the SAA region.

We estimate that a 20 pixel macropixel region encounters 3.04 hits per Nadir Mapper integration time, about 24,333 electrons, when the spacecraft passes through the peak of the SAA [10]. The error introduced by transients in Earth view radiances is the ratio of the transient signal level to the Earth view signal level. Because radiances have a large
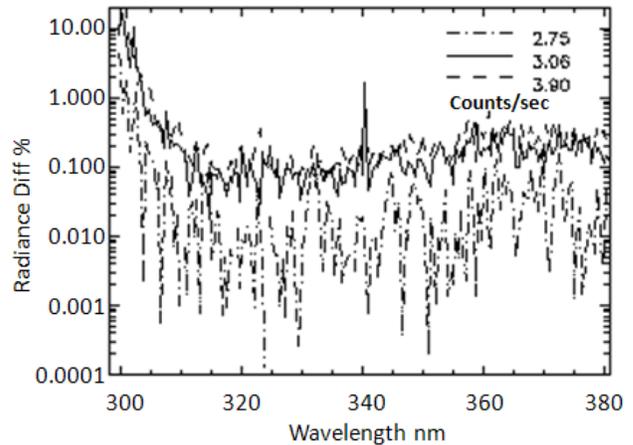
Fig. 13: Percent differences in NM Earth radiances from images that were collected when the spacecraft was crossing the SAA area at three different transient count rates.

wavelength variation, the impact is strongly wavelength dependent. Short wavelengths have the smallest signal and are most susceptible to transient errors. Fig. 13 shows an example of radiance percent differences at 3 different transient signal levels inside of SAA region. The radiance is computed using the NM orbital Earth view data. The transients that we observed in dark images cause a change in the mean dark signals from 2.75 ~ 3.9 counts/second. The overall error introduced inside of the SAA region is less than 0.2% for wavelength greater than 300 nm, but the error at short wavelengths less than 300 nm could be as great as 15%.

3.4 Random Telegraph Signals

One condition that can result from lattice damage in the flight environment is a type of behavior known as Random Telegraph Signals (RTS) [11]. The RTS pixels exhibit unstable, or quasi-stable, dark current levels, and jump between two or more discrete energy levels with some roughly characteristic time constant. RTS effects are important as their unpredictability complicates on-orbit dark current calibration and the time constants are a driver of dark update frequency requirements. Fig. 14 illustrates examples of four individual RTS pixels from OMPS NM and NP CCDs. The first three have settled into sets of more or less quasi-stable states, fairly typical RTS behavior, while the fourth displays an exponential-like decay and has not yet settled down. It is estimated that at the early orbit calibration phase, less than one tenth to several tenths percent pixels in NP and NM exhibit RTS behavior. Due to their small population, these RTS pixels can be still used in the Earth view measurement.

3.5 Detector Gains

An OMPS detector gain is determined as the number of
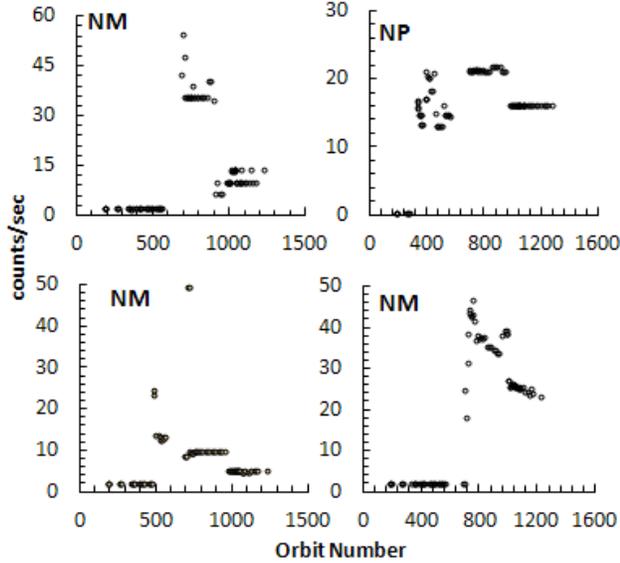
Fig. 14: Examples from four different pixels of RTS observed from sensor NM and NP dark images over time.

electrons corresponding to one analog count of the analog to digital converter. Since there is no specific orbital measurement sequence designed for calculating this quantity, we utilize a subset of the LED linearity calibration sequence to calculate gain based on the mean variance method as follows. The difference for pairs of linearity sequence reference images are calculated for each pixel. The variance of these differences is then calculated for each signal bin. The variances are linearly fit as a function of signal level, resulting in a slope of the fit that characterizes the gain. This procedure is performed for each half of the CCD FPA with its own amplifier chains.

Table 3: OMPS EOC Gains and Standard Deviations [e-/count]

Sensor	CCD	Pre-Launch		On-orbit	
		Mean	STD	Mean	STD
NP	Left	43.64	0.15	42.61	0.19
NM	Left	46.07	0.15	45.55	0.31
	Right	46.56	0.18	45.57	0.34

As results from our analyses, all of the OMPS detectors exhibit a stable gain trend with a minor offsets relative to the prelaunch predicted values. Table 3 summarizes the prelaunch and average EOC gain for each instrument. The Left and Right CCDs in the table refer to left and right halves of CCD FPA, respectively (cf. Fig. 1).

3.6 Electronic Biases

An OMPS electronic bias is calculated separately for each CCD by spatially averaging the leading or trailing serial over-clock pixels from each side of the focal plane. The number of leading and/or trailing serial over-clock pixels used in the averaging is based on the characteristics of the data obtained from acceptance testing of the integrated sensor suite in the lab. For the flight, primary electronic amplifier chains were chosen instead of the backup secondary electronics, and the central 8 of the 12 serial over-clock columns were used for orbital measurements to compare with similar lab measurements.

The orbital OMPS Nadir electronic bias that we derive from dark images for each CCD plus electronics chain agrees with the corresponding prelaunch calibration value for a difference of less than 0.2% for both the NP and NM. Fig. 15 shows a trend of the orbital NM electronic biases for the first 260 days after launch. The on-orbit bias is typically around 750 counts, which gives a total fractional uncertainty to the absolute radiance and irradiance calibrations of 0.03%. An example mean and 1-sigma STD pair from the OMPS NM is 753.50±0.12 for the left CCD (solid line) and 755.57±0.13 (dashed line) for the right CCD.
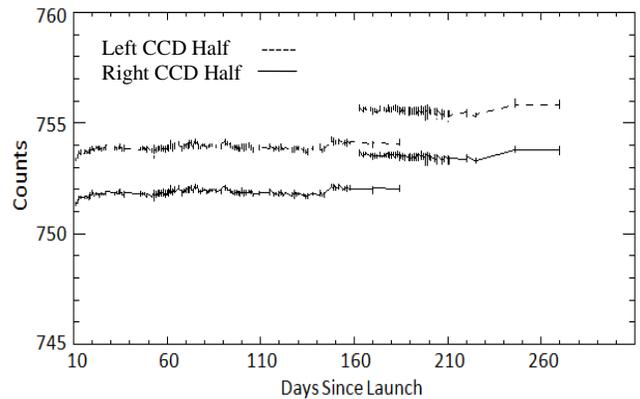
Fig. 15: For each CCD image half, the orbital OMPS NM electronic biases versus mission time. Biases are relatively stable for both types of dark image exposures of 120 sec. and 72 sec. The former time is a special diagnostic single-frame image. The later is the integration time of the newly established on-orbit dark measurement sequence.

The orbital biases in Fig. 15 were extracted from single-frame dark images collected with a special diagnostic integration time of 120 seconds for the first 150 days and an integration time of 72 seconds afterward, when the new dark calibration standard had been established. The newly established dark measurement has a slightly higher bias than before, an increase of about 0.21% on average. Nevertheless, the OMPS on-orbit primary electronic bias for each CCD read-out exhibits a stable trend over time, with a small negligible variation since launch. The orbital OMPS bias calibration is nominally performed weekly, but in case the variation becomes significant, we can compensate by adjusting the calibration frequency, even as often as a real time bias calibration for each CCD read-out.

3.7 Dark Noise

An OMPS CCD dark noise consists of combined readout noise and the dark shot-noise. The CCD dark readout noise includes all CCD-generated noise that is independent from signal and integration time. Table 4 summarizes the OMPS on-orbit readout noise mean value with 1-sigma STD for all the three CCDs. So far, all of the OMPS detectors' readout amplifiers exhibit a relatively stable behavior at levels very similar to prelaunch results. All of the orbital sensors' dark noises meet, with significant margin, the design requirement for detector noise of less than or equal to 60 e- RMS.

Table 4: NPP OMPS Readout Noise [e-]

Sensor	CCD	Pre-Launch Mean	On-orbit Mean	STD
NP	Left	28	22.7	1.4
NM	Left	23.4	24.8	1.2
	Right	25.6	24.4	1.3

We determine the readout noises from a special set of diagnostic dark quasi-images with negligible integration times. The quasi-image readouts are made from the image storage region rather than from the active image pixels, thus permitting us to measure the readout noise independently of the dark current. The resulting count levels are then converted to electrons using the relevant gains (cf. Table 3).

3.8 System Nonlinearity

The orbital OMPS linearity response is monitored monthly through an analysis of LED lamp signals measured in a series of 83 data frames with stepped integration times. The CCD exposure time increases with each even numbered lamp data frame, which is interleaved with a constant 0.5 sec reference exposure for odd numbered frames. Fig. 16 illustrates sampled counts for the entire 83 image measurement sequence. Counts from each of these LED images are collected using a pre-defined pixel sample table in order to provide uniformity of illumination.

The OMPS sensors have demonstrated highly consistent linearity so far since launch. The on-orbit performance is exceptional stable and agrees well with the prelaunch prediction. Fig. 17 shows the NM on-orbit maximum nonlinearity over the sensor entire dynamic range as a function of time since launch. As one can see, the nonlinearity is about 0.39 for the NM and is 0.32 for the NP; the linear fitting RMS is 0.07% for the NM and is 0.02% for the NP. In comparison, the sensitivity of the nonlinearity calibration is less than about 0.04% each for the NM and for the NP.

The OMPS sensors have demonstrated highly consistent linearity so far since launch. The on-orbit performance is
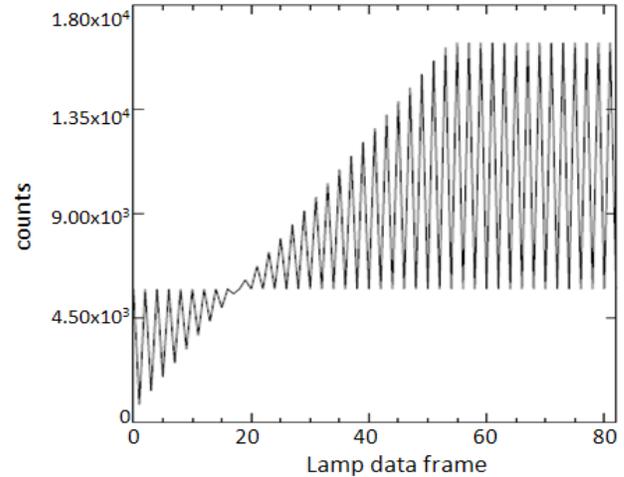
Fig. 16: Example of counts derived from an 83 image set of LED Lamp data frames that are collected in sequence during an orbital NM linearity calibration. Counts attain saturation levels at frame number 54.
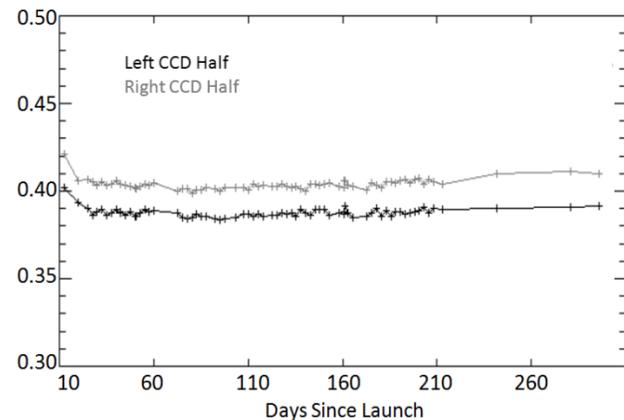
Fig. 17: The OMPS NM maximum nonlinearity per calibration versus time since launch. Each joint system of CCD plus electronics exhibits an extremely stable, nearly constant, behavior.

exceptional stable and agrees well with the prelaunch prediction. Fig. 17 shows the NM on-orbit maximum nonlinearity over the sensor entire dynamic range as a function of time since launch. As one can see, the nonlinearity is about 0.39 for the NM and is 0.32 for the NP; the linear fitting RMS is 0.07% for the NM and is 0.02% for the NP. In comparison, the sensitivity of the nonlinearity calibration is less than about 0.04% each for the NM and for the NP.

The instability of an LED's outputs during the linearity measurement complicates the linearity calibration but can be corrected using the LED reference measurements. By analyzing counts from this reference set of images, we have observed a 0.35% decrease in the lamp output over 7 minutes. This decrease in brightness must be removed in order to derive an accurate linearity calibration. The root cause of the lamp signal drift, identified during the prelaunch characterization of the sensor, was the tendency

of an LED as time passed to release fewer photons for the CCD to detect. Moreover, lab testing found that the LED output high-frequency noise randomly changes over time. Consequently, for processing of the orbital stepped integration lamp data, we routinely fit a local quadratic to the average count levels in the reference images as a function of time stamp. We then use the derived function to determine the normalizing weights to be applied to the ramped integration times to compensate for any lamp output drifting.
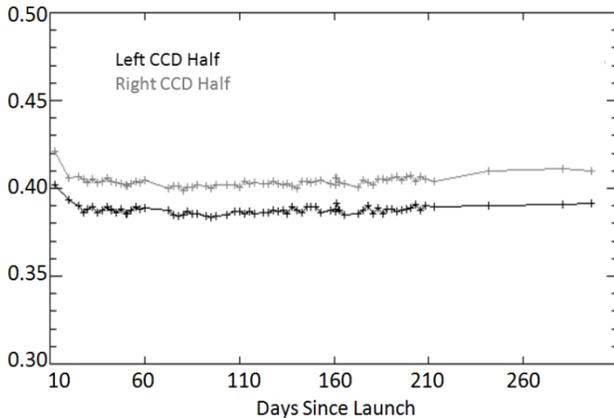
Figure 17: The OMPS NM maximum nonlinearity per calibration versus time since launch. Each joint system of CCD plus electronics exhibits an extremely stable, nearly constant, behavior.

3.9 Observed Solar Irradiance

We conduct the orbital OMPS observations of the Sun by moving the working diffuser through seven different positions and by calibrating each resulting solar image with a goniometry coefficient computed from the angle of the solar ray striking the diffuser. After combing the images into one, averaging spatially across the detectors, we compare the observed solar irradiance with the synthetic irradiance predicted from prelaunch calibration. The synthetic solar irradiance is computed by applying the prelaunch sensor band-passes to a high-spectral-resolution reference solar spectrum based on ATLAS SUSIM [8, 12] and Kitt Peak National Solar Observatory [6] (also used for Aura/OMI [13]). The current OMPS solar irradiance is updated with the orbital observed data.

Figure 18 shows that the solar spectrum observed from the orbital sensors falls almost exactly onto the predicted spectrum. We measure the differences between the orbital and predicted spectra for the NM to be within 1.22%, on average, but with ±2.4% smaller scale variations. Alternately for the NP, the observed minus predicted irradiance differences are on average less than 1.6% ± 4.5%. In the wavelength overlap region bounded by two vertical lines in Figure 18, where the wavelength varies from about 299 nm to 311 nm, the on-orbit observed solar irradiances

from the NP and the NM show a relatively large discrepancy from 0.2 to 12.19%, and the difference tends to increase with toward longer wavelengths in the overlap. The poor agreement between the two sensors in the overlap area is also found in Earth view radiances, and the root cause is yet to be understood.
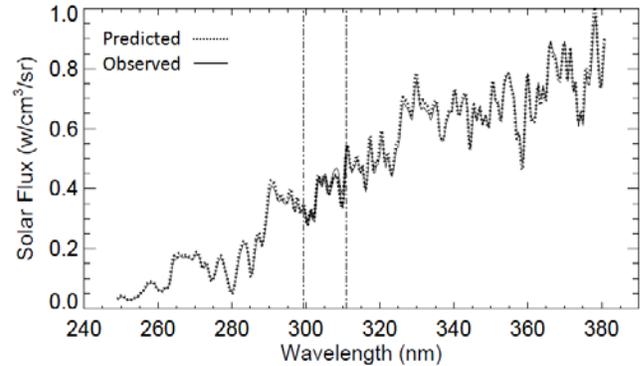
Figure 18: Comparison of the observed solar irradiance with the synthetic irradiance predicted from the prelaunch wavelength and band-pass calibrations. The spectral wavelength between the two vertical lines is shared by NP (less than 311 nm) and NM (more than 299 nm).

A study of the in-flight FWHM of the band-passes determination is currently underway but incomplete. The orbital performance of the OMPS spectral response is likely to be dominated by thermal broadening of the orbital band-pass shapes because the prelaunch calibrations revealed that the Nadir NM band-pass FWHM broadens as bulk temperature decreases. The lab band-pass FWHM increase was spatially-dependent, with a maximum increase about 10% at the center of the NM FOV. In contrast, no significant change to the NP FWHM was observed in the lab. Root cause analyses attributed the NM band-pass broadening mostly to instrument slits, which changes their size and thus the throughput of the instrument. The broadening causes 0.6 - 2.9% ozone measurement error. Correction for mean ground-to-orbit temperature change is about 2.20% when the mean change in a slit temperature from lab calibration to orbital operation is -22.5°C. The sensor allocation is for a 2% change so some margin will be needed to accommodate the exceedance.

3.10 Wavelength shift

The orbital OMPS wavelength shift for a solar spectral image is computed, pixel by pixel, within each wavelength channel by using the Levenberg-Marquardt non-linear least squares fit [14] between the observed and the synthetic solar spectra. The synthetic solar spectrum is obtained by convolving the lab band-passes with the high-resolution reference spectrum discussed in section 3.9. A map of the spectral band-pass shapes and centroid wavelengths at each pixel is used to bound the wavelength interval over which each band-pass spectral function is applied to the prelaunch

reference solar spectrum. The free parameters to the fit are the FWHM, and the linear wavelength shift varying with wavelength across the spectrum. In practice, a constant shift at all wavelengths results from our analysis.

However, besides the shift when the sensors are at the top of an orbit during solar calibration, intra-orbital wavelength shifts among Earth view observations can result from thermal variations to the sensor as it orbits with varying heating by the Sun. Less than -0.16 nm wavelength shifts is allocated when sensor was transitioned from ground to orbit. The averaged wavelength shifts for the major ozone channels are listed in Table 5.

Table 5: OMPS Nadir Wavelength Shift for Major Ozone Channels

Wavelength (nm)	Shift (nm)
253.09	-0.058
272.84	-0.092
283.02	-0.114
288.14	-0.092
291.99	-0.086
297.99	-0.094
301.86	-0.109
306.17	-0.136
312.84	-0.114
317.86	-0.117
330.80	-0.118
339.97	-0.115
380.02	-0.093
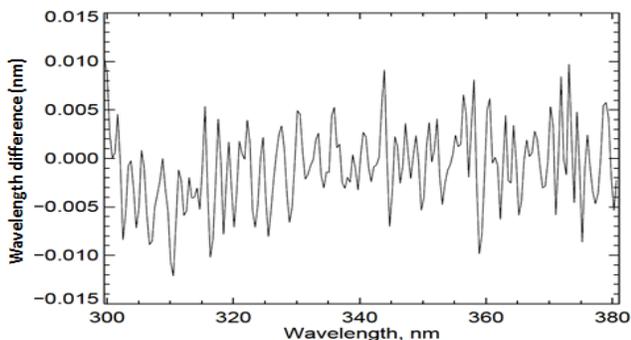
Figure 19: Time-Averaged wavelength shifts in nm from 14 orbits of Earth data on July 04, 2012. The variation of the Nadir telescope housing temperature is about 1.3 degrees.

Figure 19 captures NM intra-orbital wavelength shifts caused by the variations in OMPS optical bench temperatures. Empirical Orthogonal Functions (EOF) Covariance Analysis [15] was applied to the NM for the central cross-track position for the 300 nm to 380 nm wavelength ranges for 14 orbits on 07/04/2012. The figure shows the sum of the first two EOF patterns and also has the

computed variations expected from a 0.02-nm wavelength shift produced by intra-orbital variations in the optical bench temperatures. While the shifts are small (within 0.013 nm) and meet our expectation, we plan to implement a correction to improve the ozone products.

4. SUMMARY

OMPS made a smooth transition from ground to orbit. The on-orbit CCD detector performance meets our predicted level and agrees with the prelaunch values determined during the prelaunch calibration and characterization. Our OMPS orbital characterizations of detector performance show that the sensors' electronic bias, detector gain, dark smear, dark current rate, and linearity remain within 0.2% of the prelaunch values with significant margin below sensor requirements. Detector gain and bias performance trends are generally stable. System linearity performance exhibits excellent stability and is highly consistent with the prelaunch values. When compared with synthetic data, our solar observations confirm the validity of the orbital radiometric calibration except for the NP in the wavelength overlap with the NM. Changes in dark current due to transients and hot pixels are within our expectations and a more frequently update of the dark calibration table has been scheduled.

5. REFERENCES

[1] J. V. Rodriguez, et al., "An Overview of the Nadir Sensor and Algorithms for the NPOESS Ozone Mapping and Profiler Suite (OMPS)," *Proc. SPIE*, 4891, April 2003; DOI: 10.1117/12.467525.

[2] M. G. Dittman; E. Ramberg; M. Chrisp; J. V. Rodriguez; A. L. Sparks, et al. "Nadir Ultraviolet Imaging Spectrometer for the NPOESS Ozone Mapping and Profiler Suite (OMPS)," *Proc. SPIE*, 4814, Earth Observing Systems VII, p. 111, September 25, 2002; DOI: 10.1117/12.453748

[3] Q. P. Remund, et al., "The Ozone Mapping and Profiler Suite (OMPS): on-orbit calibration design," *Proc. SPIE*, 5652, pp. 165–173, December 2004; DOI: 10.1117/12.579016.

[4] C. J. Seftor, J.C. Larsen, T. J. Swissler, J. V. Rodriguez, Q. Remund., G. Jaross, and C. G. Wellemeyer, "OMPS Total Column Algorithm Performance: Comparison to TOMS and to NPOESS Requirements," *Proc. SPIE* 4891, pp. 1–12, 2003.

[5] K. Chance, "Analysis of BrO Measurements from the Global Ozone Monitoring Experiment," *Geophys. Res. Lett.*, 25, p. 3335, 1998.

[6] R. L. Kurucz, I. Furenlid, J. Brault, and L. Testerman, "Solar Flux Atlas from 296 to 1300 nm," *National Solar Observatory*, Sunspot, New Mexico, p. 240, 1984.

[7] L.A. Hall and G.P. Anderson, "High-Resolution Solar Spectrum Between 200 and 3100 Å," ," *J. Geophys. Res*. 96, 12, pp. 927–931, 1991.

[8] T.N. Woods, D.K. Prinz, G.J. Rottman, J. London, P.C. Crane, R.P. Cebula, E. Hilsenrath, G.E. Brueckner, M.D. Andrews, O.R. White, M.E. VanHoosier, L.E. Floyd, L.C. Herring, B.G. Knapp, C.K. Pankratz, and P.A. Reisner,

"Validation of the UARS Solar Ultraviolet Irradiances: Comparison with the ATLAS 1 and 2 Measurements," *J. Geophys. Res*. 101, pp. 9541–9569, 1996.

[9] C. Caspar and K. Chance, "GOME Wavelength Calibration Using Solar and Atmospheric Spectra," *Proc. 3rd ERS Symposium, Space at the Service of our Environment*, pp. 609–614, 1997.

[10] Q. P. Remund, "SAA Impacts on Nadir Mapper and Limb Profile EDR Performance", *System Engineering Report*, Ball Space and Technologies Corporation, pp. 2–3, October 8 2003.

[11] I. H. Hopkins and G. R. Hopkinson, "Random Telegraph Signals from Proton-Irradiated CCDs," *IEEE Trans. Nucl. Sci.*, vol. 40, no. 6, pp. 1567–1574, December 1993.

[12] G. E. Brueckner, K. L. Edlow, L. E. Floyd IV, J. L. Lean and M. E. VanHoosier, "The Solar Ultraviolet Spectral Irradiance Monitor (SUSIM) Experiment on board the Upper Atmosphere Research Satellite (UARS)", *J. Geophys. Res.,* vol. 98, No. D6, p. 10, 695, 1993; DOI: 10.1029/93JD00410

[13] P.F. Levelt, G.H.J. van den Oord, M.R. Dobber, A. Mälkki, H. Visser, J. de Vries, P. Stammes, J. Lundell, and H. Saari, *"The Ozone Monitoring Instrument", IEEE Trans. Geo. Rem. Sens.*, Vol. 44**,** No. 5, 1093–1101, 2006; DOI:10.1109/TGRS.2006.872333.

[14] W. H. Press, B. P. Fleming, S. A. Teukolsky, and W. T. Vetterling, *Numerical Recipes*, Cambridge University Press, New York, NY, USA, pp. 523–525, 1986.

[15] G. R. North, T. L. Bell, R. F. Cahalan, and F. J. Moeng, "Sampling Errors in the Estimation of Empirical Orthogonal Functions," *Mon. Wea. Rev.*, 110, pp. 699–706, 1982.